

Pseudospin dynamics of exciton-polariton patterns in a coherently driven semiconductor microcavity

Albrecht Werner, Oleg A. Egorov, and Falk Lederer

Institute of Condensed Matter Theory and Solid State Optics, Abbe Center of Photonics, Friedrich-Schiller-Universität Jena, Max-Wien-Platz 1, 07743 Jena, Germany

(Received 11 July 2014; revised manuscript received 2 October 2014; published 23 October 2014)

The influence of the exciton spin on the formation and stability properties of periodic cavity polariton patterns is studied in a semiconductor microcavity operating in the strong-coupling regime. A linearly polarized optical beam excites polaritons formed by excitons with different spin orientations and left- and right-circularly polarized photons. The perturbation analysis of homogeneous solutions reveals a competition between these two spin states. The outcome of this competition is determined by the sign of the cross-phase modulation parameter. In particular, it is shown that linearly polarized patterns are preferred, if this parameter is positive. Otherwise, a spontaneous symmetry-breaking instability leads to the formation of transverse patterns with a spatial polarization asymmetry. In the regime of bistable homogeneous solutions we observe the spontaneous formation of domains framed by one-dimensional dark half solitons.

DOI: [10.1103/PhysRevB.90.165308](https://doi.org/10.1103/PhysRevB.90.165308)

PACS number(s): 42.65.Sf, 42.65.Pc, 71.36.+c, 47.20.Ky

I. INTRODUCTION

We consider a semiconductor multiple quantum well in a high- Q microcavity. The strong coupling of semiconductor excitons with cavity photons leads to the formation of new quasiparticles which are termed exciton-polaritons [1–4]. Exciton-polaritons therefore bear both photonic and excitonic properties, which makes them particularly interesting for all-optical information storage and processing applications [5,6]. In particular, they experience diffraction mainly due to their photonic nature and inherit the strong and fast nonlinearity arising from the Coulomb interaction between excitons. The interplay between these two properties can lead to the formation of extended periodic spatial patterns which arise spontaneously from an initially uniform field. After the pioneering work in fluid dynamics, pattern formation has been studied in various nonlinear systems reaching from solid-state physics over chemical reaction dynamics to self-assembly in biological systems [7,8]. Based on the well-established theoretical model for an optical Kerr cavity [9], various theoretical and experimental investigations of pattern formation in this environment have been a topic of vigorous interest during the past 25 years [9–16].

Along with other classical issues of nonlinear dynamics, recently the formation of periodic patterns was studied in polaritonic systems, too [17–20]. In Refs. [17–19] the pattern dynamics of spinless exciton-polaritons was investigated. Unlike those works, the influence of the exciton spin on the pattern dynamics is in the focus of the present contribution. Another aspect of the polarization dynamics related to the TE-TM splitting between the cavity modes was considered in Refs. [20,21].

Ground-state excitons in quantum wells consist of an electron with spin $\pm 1/2$ and a heavy hole with spin $\pm 3/2$ [22–25]. The four allowed projections of the exciton spin on the structure growth axis are therefore ± 1 and ± 2 . The former can be optically excited by photons carrying left- or right-circular polarization. States with spin ± 2 , however, cannot be excited by single photons. Therefore their contribution to the formation of exciton-polaritons is negligible and they are

called dark states. However, they are indirectly involved, since bright-state excitons with opposite spins can interact via virtual dark-state excitons [22,26]. The inclusion of the spin degree of freedom results in various polarization phenomena such as polarization multistability [27–29], spin rings [30,31], spin switching [32,33], half quantum vortices [34], half solitons, or dissipative vector solitons [35–39].

It turns out that the polariton equations with exciton spin exhibit the same structure in the nonlinearity as the equations of motion of a vectorial Kerr cavity [13,14]. Therefore several results derived there that arise from the vectorial character of the problem will be addressed in the present contribution.

The cross-phase modulation parameter α between the two spins can have either sign [25,29,35,40]. In Ref. [39] the authors showed that for $\alpha < 0$ the spontaneous symmetry breaking between the two spin components of a dark polariton soliton evokes a spatial splitting between these two components. Similar effects will appear for periodic patterns: Whereas for $\alpha > 0$ a linearly polarized solution consisting of two identical polarization patterns is expected, for $\alpha < 0$ the spontaneous symmetry breaking manifests itself in the formation of two spatially shifted polarization patterns associated with opposite exciton spins.

This paper is organized as follows. In Sec. II we introduce the equations of motion for exciton-polaritons with spin. In Sec. III we study the behavior of homogeneous solutions to these equations by means of a linear stability analysis thus surveying the occurrence of the symmetry-breaking instability for $\alpha < 0$. This analysis represents the backbone for our further numerical simulations which are presented in Sec. IV. This section contains a comparison of the formation of linearly polarized patterns for $\alpha > 0$ and patterns with space-dependent elliptical polarization degree for $\alpha < 0$. In Sec. V a mechanism is presented that circumvents the frustration of hexagonal pattern formation in the bistable domain by means of the spontaneous buildup of domains framed by one-dimensional dark half solitons.

II. MATHEMATICAL MODEL

The dimensionless mean-field equations for the left (E^+) and right (E^-) circularly polarized components of the photonic field coupled to the excitonic fields (Ψ^\pm) with spins ± 1 read as [3,4,25]

$$\begin{aligned} \partial_t E^\pm - i\nabla_\perp^2 E^\pm + (\gamma_c - i\Delta_c)E^\pm &= i\Psi^\pm + E_p, \\ \partial_t \Psi^\pm + (\gamma_0 - i\Delta_0)\Psi^\pm + i(|\Psi^\pm|^2 + \alpha|\Psi^\mp|^2)\Psi^\pm &= iE^\pm. \end{aligned} \quad (1)$$

Here, E and Ψ stand for the averages of photon and exciton annihilation operators, respectively. Normalization is chosen such that $(\Omega_R/g)|E^\pm|^2$ and $(\Omega_R/g)|\Psi^\pm|^2$ denote the photon and exciton numbers per unit area, where Ω_R is the frequency of the Rabi oscillations and g the nonlinear interaction constant of excitons with equal spin. The strength of the cross-phase modulation between different spin states is described by the dimensionless parameter α [25,29,35,40]. E_p denotes the coherent linearly polarized optical pump and $\Delta_{c,0} = (\omega - \omega_{c,0})/\Omega_R$ are the normalized detunings of the pump frequency ω from the resonance frequencies ω_c of the cavity and ω_0 of the excitons, respectively. In our numerical simulations in Secs. IV and V we shall choose both detunings identical and shall denote this quantity by Δ . For some of the analytical results in Sec. III, however, it is reasonable to stress the difference between Δ_0 and Δ_c . The damping constants γ_0 and γ_c of excitons and cavity are also normalized to Ω_R . The transverse Laplacian $\nabla_\perp^2 = \partial_x^2 + \partial_y^2$ and the corresponding transverse coordinates x and y are scaled by $x_0 = \sqrt{c/(2nk\Omega_R)}$, where n denotes the refractive index and $k = n\omega/c$ is the wave number. The external pump is normalized such that the incident pump intensity is $I_{\text{inc}} = \hbar\omega\Omega_R^2|E_p|^2/g\gamma_c$ [41]. In a microcavity with a single InGaAs/GaAs quantum well, realistic parameters are $\hbar\Omega_R \approx 2.5$ meV and $\hbar g \approx 10^{-4}$ meV. A unit of time in Eqs. (1) corresponds to ≈ 0.25 ps for this choice of parameters. Assuming that the typical relaxation times of the photonic and excitonic field are 2.5 ps we used $\gamma_c \approx \gamma_0 \approx 0.1$ for all calculations below. Therefore one unit of the normalized time t amounts to 0.1 photon lifetimes. We denote the total intensity of the photon field by $I_E = |E^+|^2 + |E^-|^2$ and its polarization degree by $\rho_E = (|E^+|^2 - |E^-|^2)/I_E$.

Since the linearly polarized optical pump acts on both polarizations equally, the equations of motion are invariant with respect to the permutation of $+$ and $-$ fields. Therefore, two types of solutions are possible. *Symmetric* solutions ($\rho_E = 0$) are expected to share many properties of the scalar solutions described in Ref. [19]. However, within the scope of this paper, we will mainly deal with *asymmetric* solutions ($\rho_E \neq 0$) arising after the spontaneous breaking of the spin symmetry of our model (1). It will be shown comprehensively that these solutions develop several novel properties reinforcing the strong-coupling properties separating the polaritonic system from conventional nonlinear cavities [14].

III. ANALYSIS OF HOMOGENEOUS SOLUTIONS

Before discussing transverse effects, we are going to explore some properties of stationary plane wave solutions of Eqs. (1), which will be termed homogeneous solutions

(HSs). Similar to the scalar case, the symmetric HSs are bistable for an appropriate choice of the detunings [19,42]. The bifurcation of asymmetric HSs and the corresponding polarization multistability phenomena were studied analytically in [27,28,39] and experimentally in [29]. These works show the HSs to be a prototypical example for the coexistence of symmetric and asymmetric solutions at the same pump power.

Spatial patterns arise when a control parameter exceeds its critical value and the HSs destabilize in favor of spatially periodic solutions. This destabilization mechanism arises from the interplay between diffraction and nonlinearity and is termed after Turing crediting his pioneering efforts [43] in the framework of pattern formation in biochemical systems. It is commonly referred to as modulation instability (MI).

In what follows a quantitative analytical description of these destabilization processes is provided. Since a linearly polarized pump is applied, the unperturbed HSs can be expected to be linearly polarized, too: $E_0^+ = E_0^- =: E_0$ and $\Psi_0^+ = \Psi_0^- =: \Psi_0$. The common scheme for spatially varying perturbations on top of the HSs and their complex conjugate fields \bar{E}_0 and $\bar{\Psi}_0$ reads as

$$\begin{aligned} E^\pm &= E_0 + \varepsilon_1^\pm e^{\lambda t} e^{i(k_x x + k_y y)}, \\ \bar{E}^\pm &= \bar{E}_0 + \varepsilon_2^\pm e^{\lambda t} e^{-i(k_x x + k_y y)}, \\ \Psi^\pm &= \Psi_0 + \psi_1^\pm e^{\lambda t} e^{i(k_x x + k_y y)}, \\ \bar{\Psi}^\pm &= \bar{\Psi}_0 + \psi_2^\pm e^{\lambda t} e^{-i(k_x x + k_y y)}, \end{aligned} \quad (2)$$

where the perturbation amplitudes $\varepsilon_1, \varepsilon_2, \psi_1, \psi_2$ are independent in the ansatz (2). Since the equations of motions are isotropic in the x - y plane, all quantities depend only on the squared modulus $k^2 = k_x^2 + k_y^2$ of the transverse wave vector $\mathbf{k} = (k_x, k_y)^T$ rather than on its very components. The quantity $|\Psi_0|$ and the related polaritonic intensity $I_0 = |\Psi_0|^2$ are suitable candidates for the system's control parameter rather than the pump power. Plugging the ansatz (2) in the equations of motion (1) and linearizing the occurring equations in the perturbations leads to a homogeneous system of eight algebraic equations, which can be formulated as an eigenvalue problem in λ . It decouples into a symmetric ($\varepsilon_2 = \varepsilon_1, \psi_2 = \psi_1$) and an antisymmetric ($\varepsilon_2 = -\varepsilon_1, \psi_2 = -\psi_1$) part. This decoupling was also reported for vectorial Kerr cavities [14].

The separation of symmetric and asymmetric modes simplifies the further analytical considerations significantly, since the 8-by-8 eigenvalue matrix decouples into two 4-by-4 matrices for the symmetric and the antisymmetric part, respectively. As long as the real part of all four eigenvalues is negative, the HS is stable with respect to the regarded perturbations. When the control parameter exceeds its critical value, at least one of these eigenvalues exhibits a positive real part for a certain $k = |\mathbf{k}|$. Usually this quantity is denoted as *growth rate* $\text{Re}\lambda(k, |\Psi_0|)$. Here one has to distinguish between the growth rate $\text{Re}\lambda_s(k, |\Psi_0|)$ for symmetric modes and $\text{Re}\lambda_{\text{as}}(k, |\Psi_0|)$ for asymmetric ones. Periodic solutions of Eqs. (1) are amplified, if their wave vector obeys the condition $\text{Re}\lambda(k, |\Psi_0|) > 0$. This leads to the spontaneous formation of spatial patterns arising from a modulationally unstable HS.

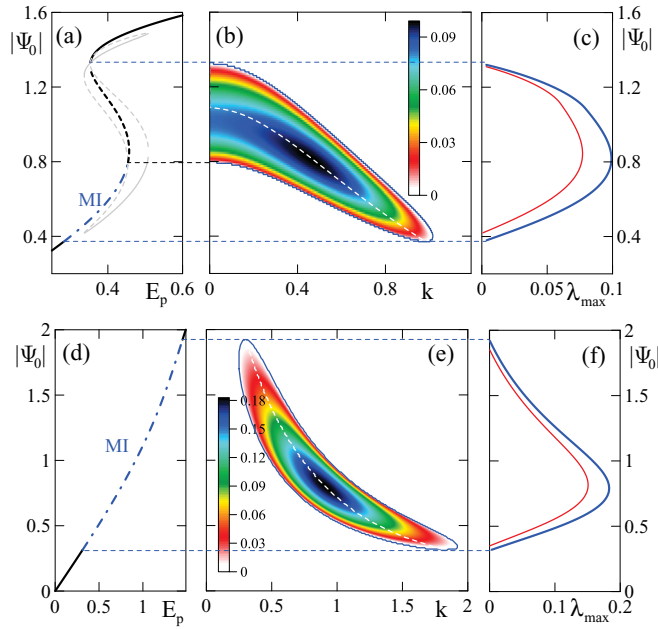


FIG. 1. (Color online) (a)–(c) Analysis of homogeneous solutions (HSs) for $\alpha = -0.1$ with $\Delta = -0.45$: (a) HS branches $|\Psi^\pm|$ over the pump power E_p : symmetric HSs (bold black), asymmetric HSs (thin gray), and MI range (blue chain line). Continuous lines denote stable solutions, whereas dashed lines stand for unstable HSs; (b) growth rate $\text{Re}\lambda(k, |\Psi_0|)$, boundary of instability range $\text{Re}\lambda(k, |\Psi_0|) = 0$ (blue line) and stable domain $\text{Re}\lambda(k, |\Psi_0|) < 0$ (white area); (c) maximal growth rates $\text{Re}\lambda_s(k, |\Psi_0|)$ and $\text{Re}\lambda_{as}(k, |\Psi_0|)$ for a given order parameter $|\Psi_0|$ of symmetric (thin red) and antisymmetric (bold blue) perturbations, respectively. The dashed white line in (b) shows the position of $\text{Re}\lambda_{\max}(k, |\Psi_0|)$ in the k - $|\Psi_0|$ plane. Horizontal dashed lines denote the onset and the cessation of the modulational instability. (d)–(f) show the respective figures for $\alpha = -0.1$ with $\Delta = -0.1$.

For $\alpha < 0$ the growth rate of the asymmetric modes always exceeds that of the symmetric modes: $\text{Re}\lambda_{as}(k, |\Psi_0|) > \text{Re}\lambda_s(k, |\Psi_0|)$. This scenario is exemplarily shown for $\alpha = -0.1$ with detunings $\Delta = -0.45$ in Figs. 1(a)–1(c) and $\Delta = -0.1$ in Figs. 1(d)–1(f). At first, the case $\Delta = -0.1$ will be studied, where the symmetric HSs are monostable. Figure 1(e) displays the growth rate $\text{Re}\lambda(k, |\Psi_0|) = \text{Re}\lambda_{as}(k, |\Psi_0|)$. The branch of modulationally unstable HSs is shown in Fig. 1(d). For each value of the control parameter $|\Psi_0|$ there is a value of the wave vector k , where the growth rate takes its maximum $\text{Re}\lambda_{\max}$. The k value at $\text{Re}\lambda_{\max}$ determines the typical period of the arising pattern. In Fig. 1(f) we show that the maxima of $\text{Re}\lambda_{as}(k, |\Psi_0|)$ are larger than that of $\text{Re}\lambda_s(k, |\Psi_0|)$ for all values of $|\Psi_0|$. Therefore all arising patterns are expected to be governed by the dynamics arising from the antisymmetric modes.

Another scenario arises for bistable symmetric HSs, for example by choosing $\Delta = -0.45$; cf. Figs. 1(a)–1(c). In this case, there is an additional $|\Psi_0|$ range where the HS destabilizes against perturbations with $k = 0$. Usually this does not lead to the formation of transverse patterns but rather to a spontaneous switching to the stable upper branch of the bistability loop and was therefore termed bistable frustration [11]. This range is indicated by a bold black dashed line in Fig. 1(a). It will be examined in Sec. V.

The corresponding scenario for positive α is quite different. It shows the dominance of the symmetric modes and therefore $\alpha > 0$ leads to the formation of stable symmetric patterns.

One can conclude that for $\alpha < 0$ ($\alpha > 0$) there is a critical $|\Psi_0|$ range where solely asymmetric (symmetric) modes are amplified. In the following, analytical expressions for the respective critical quantities will be derived. For symmetric perturbations, the critical intensity $I_{0,\text{crit},s}^\pm$ at the Turing instability points amounts to

$$I_{0,\text{crit},s}^\pm = \frac{1 + 4\gamma_c \Delta_0 \pm \sqrt{1 - 4\gamma_c [3\gamma_0(1 + \gamma_0\gamma_c) - \Delta_0(2 + \gamma_c\Delta_0)]}}{6\gamma_c(1 + \alpha)}, \quad (3)$$

whereas for antisymmetric perturbations we get

$$I_{0,\text{crit},as}^\pm = \frac{1 - \alpha + 4\gamma_c \Delta_0 \pm \sqrt{(1 - \alpha + 4\gamma_c \Delta_0)^2 - 4(3 - \alpha)(1 + \alpha)\gamma_c(\gamma_0 + \gamma_0^2\gamma_c + \gamma_c\Delta_0^2)}}{2(3 - \alpha)(1 + \alpha)\gamma_c}. \quad (4)$$

The wave vectors of the asymmetric patterns at this bifurcation point fulfill the relation

$$(k_{\text{as}}^\pm)^2 = \Delta_c + \frac{(1 - \alpha)(1 + 2\gamma_0\gamma_c) \mp \sqrt{(1 - \alpha + 4\gamma_c \Delta_0)^2 - 4(3 - \alpha)(1 + \alpha)\gamma_c(\gamma_0 + \gamma_0^2\gamma_c + \gamma_c\Delta_0^2)}}{4\gamma_0 - 2(1 - \alpha)\Delta_0}. \quad (5)$$

Equations (4) and (5) are only valid for $(k_{\text{as}}^\pm)^2 \geq 0$. For detunings leading to $(k_{\text{as}}^\pm)^2 < 0$ we set $(k_{\text{as}}^\pm)^2 = 0$. Then the critical intensity at the upper bifurcation point reads as

$$I_{k=0,\text{crit},as}^\pm = \frac{-2\mathcal{B} \pm \sqrt{4\mathcal{B}^2 - [4 - (1 - \alpha)^2](\mathcal{B}^2 + \mathcal{A}^2)}}{4 - (1 - \alpha)^2}, \quad (6)$$

where $\mathcal{A} = \gamma_0 + \gamma_c/(\gamma_c^2 + \Delta_c^2)$ and $\mathcal{B} = -\Delta_0 + \Delta_c/(\gamma_c^2 + \Delta_c^2)$. It should be noted that $I_{0,\text{crit},as}^\pm$ does not depend on Δ_c

whereas $I_{k=0,\text{crit},as}^\pm$ depends on both detunings and was already calculated in Ref. [39].

In Eqs. (3)–(6) the $-/+$ signs do not refer to the exciton spin but to the lower and upper destabilization point of the HSs, respectively. The main results of the above analysis are illustrated in Fig. 2. In Fig. 2(a) we plotted the critical intensity $I_{0,\text{crit}}^-$ over α at $\Delta_0 = -0.45$ for both symmetric and antisymmetric perturbations. It can be seen that for $\alpha > 0$ the MI point for symmetric perturbations lies at a smaller pump power than that of the antisymmetric perturbations. This

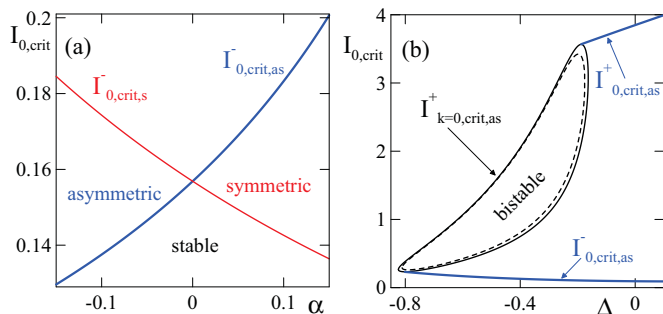


FIG. 2. (Color online) Results of the perturbation analysis of homogeneous solutions: (a) critical intensity for symmetric (thin red) and antisymmetric perturbations (bold blue) as a function of α for $\Delta_0 = -0.45$; (b) intensity $I_{0,crit,as}^-$ at the lower bifurcation point and $I_{0,crit,as}^+$ at the upper bifurcation point as a function of the detuning Δ for $\alpha = -0.1$ (bold blue lines); within the region encircled by the thin solid black curve also perturbations with $k = 0$ are unstable; the dashed black lines frame the range between the turning points of the bistability loop for symmetric HSs.

means that the arising patterns can be expected symmetric [$\rho_E(x,y) \equiv 0$] and each polarization is similar to the scalar hexagonal patterns from Ref. [19]. For $\alpha < 0$, however, the bifurcation point for antisymmetric perturbations lies at a smaller pump power than that for the symmetric ones. In Ref. [39] we proved for dark solitons that these antisymmetric dynamics are reflected in a spatial effect, namely in the spatial separation of the two half solitons formed in $+$ and $-$ polarization. For hexagonal patterns, this spatial breakup is also expected to appear in the form of two spatially shifted $+$ and $-$ patterns. The polarization degree $\rho_E(x,y)$ is then also nontrivial.

Figure 2(b) displays the full instability landscape for negative α . The intensity range between the inflection points of the bistability loop for symmetric HSs is framed by the dashed black contour. It is included in the range of symmetric HSs being unstable with respect to uniform perturbations which is calculated from Eq. (6) and depicted by a solid black contour. The bold blue lines denote the critical intensities $I_{0,crit,as}^\pm$ according to Eq. (4) in their existence range.

In this section the results for the symmetric (linearly polarized) case can be adopted from the results presented in Ref. [19] by scaling the scalar fields with the factor $\sqrt{1+\alpha}$.

IV. PSEUDOSPIN PATTERNS

The HS analysis in Sec. III has revealed that the expected shape of the arising patterns depends crucially on the cross-phase modulation parameter α between excitons with different spin, in particular on the sign of α . In Ref. [39] we have shown for dark solitons that this sign is the crucial parameter for the dynamics and the field configuration of the polaritonic system. Whereas for $\alpha > 0$ symmetric solitons are preferred where both polarizations form the same profile, a spontaneous symmetry breaking appears for $\alpha < 0$. Similar effects will be observed for spatially extended patterns in this section.

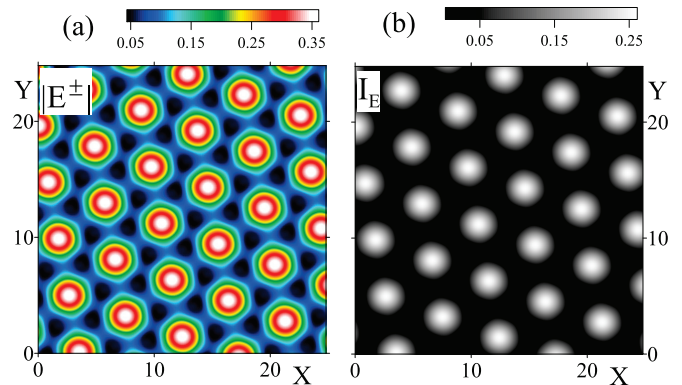


FIG. 3. (Color online) (a) Two-dimensional profile $|E^+(x,y)| = |E^-(x,y)|$ of a hexagonal pattern for $\alpha > 0$; (b) field intensity $I_E(x,y) = |E^+(x,y)|^2 + |E^-(x,y)|^2$. Parameters are $\alpha = 0.1$, $\Delta = -0.1$, and $E_p = 0.35$.

For $\alpha = 0$ the equations for both $+/-$ polaritons degenerate to two decoupled scalar equations which were already investigated [19].

For $\alpha > 0$ the two spins are coupled. Hexagonal patterns arise beyond the bifurcation point for MI. The patterns for both polarizations are identical [cf. Fig. 3(a)] which manifests itself in a linearly polarized hexagonal pattern with polarization degree $\rho_E(x,y) \equiv 0$. Therefore the location of maxima and minima of the field intensity $I_E(x,y)$ coincides with that of the respective field moduli $|E^\pm(x,y)|$; cf. Fig. 3(b). This symmetric pattern fulfills the prediction from Sec. III where its shape was deduced from the fact that the symmetric perturbations are preferred compared with the antisymmetric ones for $\alpha > 0$. These symmetric patterns do not exhibit any novel properties in comparison with the scalar patterns studied in Ref. [19].

For the physically more relevant case $\alpha < 0$, however, antisymmetric perturbations are dominating. This is reflected by a spontaneous spatial shift between the patterns of the two polarizations similar to the spatial splitting between dark solitons reported in Ref. [39]. In Fig. 4 a prototypical example near $I_{0,crit,as}^-$ for $\Delta = -0.1$ is studied. Figure 4(a) shows the total field intensity $I_E(x,y)$. Although being hexagonal, the arising intensity pattern differs substantially from the intensities of the single polarizations, because the spatial splitting between the two hexagonal lattices is not small but rather in the same order of magnitude as the lattice spacing. $I_E(x,y)$ can be classified as honeycomb-like, despite being formed by two hexagonal patterns $|E^+(x,y)|$ and $|E^-(x,y)|$. The spatial shift between these two patterns is indicated by the black and white hexagon indicating the maxima of $|E^+(x,y)|$ and $|E^-(x,y)|$, respectively. It manifests itself in the nontrivial polarization degree $\rho_E(x,y)$ depicted in Fig. 4(b). The spatial shift between the two polarizations matches with the structure of the patterns: the maxima of $|E^+(x,y)|$ coincide with the minima of $|E^-(x,y)|$ and vice versa.

A similar scenario can be observed near $I_{0,crit,as}^-$ for $\Delta = -0.45$; cf. Fig. 5. Here, $|E^+(x,y)|$ and $|E^-(x,y)|$ are shifted along a line coinciding with a basis vector of the hexagonal lattice. This changes the phenotype of the arising intensity pattern substantially. Figure 5(a) shows a striplike pattern. A

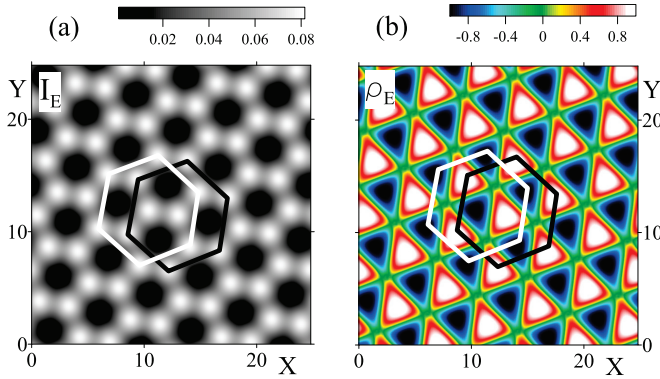


FIG. 4. (Color online) Symmetry-breaking mechanism leading to the formation of vectorial hexagonal patterns for $\alpha < 0$: (a) total intensity $I_E(x, y) = |E^+(x, y)|^2 + |E^-(x, y)|^2$ of the photon field; (b) polarization degree $\rho_E(x, y)$. The white (black) hexagon indicates the maxima of $|E^-(x, y)|$ ($|E^+(x, y)|$). Parameters are $\alpha = -0.1$, $\Delta = -0.1$, and $E_p = 0.35$.

look at Fig. 5(b) shows that both the bright and the dark stripes experience a modulation of the polarization degree. Therefore, the hexagonal nature of the pattern is preserved, at least with respect to the polarization degree $\rho_E(x, y)$.

Up to this point, we restricted our observations to the close vicinity of the bifurcation point $I_{0, \text{crit, as}}^-$ and varied mainly the detuning. However, in Ref. [19] it was shown that for, e.g., $\Delta = -0.1$ the HSs show a monostable dependence on the pump power. This makes the whole modulationally unstable pump range accessible for the formation of a variety of stable extended patterns. In Fig. 6 we present two examples for different pump powers leading to different types of stripe patterns in I_E .

Figures 6(a)–6(c) show vectorial labyrinthine patterns. From the polarization degree $\rho_E(x, y)$ in Fig. 6(c) it can be seen that there is a spatial shift between the stripes of $|E^+(x, y)|$ and $|E^-(x, y)|$. Another peculiarity is the occurrence of point defects, marked in Fig. 6(c).

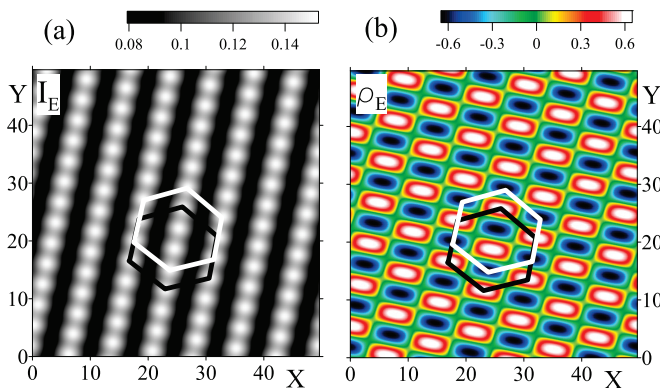


FIG. 5. (Color online) Symmetry-breaking mechanism leading to the formation of modulated stripes for $\alpha < 0$: (a) total intensity $I_E(x, y) = |E^+(x, y)|^2 + |E^-(x, y)|^2$ of the photon field; (b) polarization degree $\rho_E(x, y)$. The white (black) hexagon indicates the maxima of $|E^-(x, y)|$ ($|E^+(x, y)|$). Parameters are $\alpha = -0.1$, $\Delta = -0.45$, and $E_p = 0.2816$.

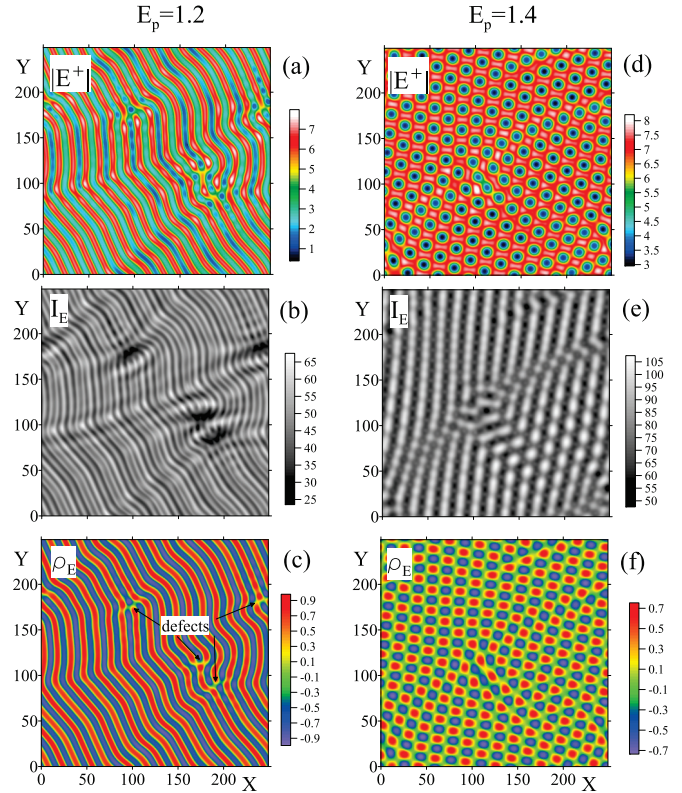


FIG. 6. (Color online) Formation of various vectorial patterns for $\alpha = -0.1$ and $\Delta = -0.1$: (a)–(c) labyrinthine stripe patterns for $E_p = 1.2$: (a) $|E^+(x, y)|$; (b) total intensity $I_E(x, y) = |E^+(x, y)|^2 + |E^-(x, y)|^2$ of the photon field; (c) polarization degree $\rho_E(x, y)$. (d)–(f) honeycomb patterns add to modulated stripes for $E_p = 1.4$: (d) honeycomb pattern $|E^+(x, y)|$; (e) striplike total intensity $I_E(x, y) = |E^+(x, y)|^2 + |E^-(x, y)|^2$ of the photon field; (f) hexagonally patterned polarization degree $\rho_E(x, y)$.

Near the upper bifurcation point $I_{0, \text{crit, as}}^-$, the field $|E^+(x, y)|$ forms a honeycomb pattern; cf. [19] and Fig. 6(d). The intensity profile in Fig. 6(e) shows several domains originating from various dislocations in the hexagonal structure of $|E^\pm|$. Whereas in the domain on the right, $I_E(x, y)$ preserves the original hexagonal structure due to impurities in the fields, the other domain shows a striplike pattern. The polarization degree $\rho_E(x, y)$ in Fig. 6(f), however, still bears the hexagonal symmetry of the original profiles.

All examples with $\alpha < 0$ in this section show genuine vectorial characteristics which cannot be observed in the framework of the scalar model [19]. Furthermore, it was shown that the additional consideration of TE-TM splitting between the cavity modes induces a spontaneous motion of the whole polariton pattern [20].

In Ref. [14] the formation of stripe patterns with uniform polarization degree along each stripe was reported for a vectorial Kerr cavity. However, in order to match the parameters used there in the polaritonic system studied here, one would have to choose $\alpha = 7$, which lies outside the physical range yet known for this parameter.

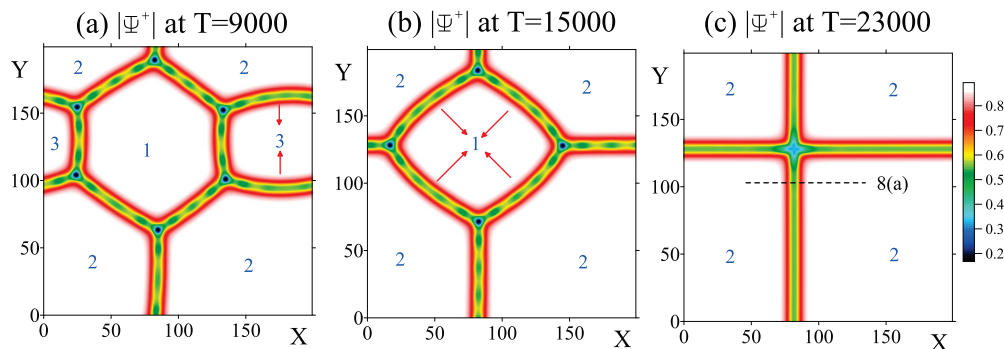


FIG. 7. (Color online) Formation of a domain structure separated by multiple one-dimensional dark half solitons for $\Delta = -0.7$, $\alpha = -0.1$, and $E_p = 0.19$: (a) three spatially distinct domains (enumerated by 1 to 3) are separated by slowly moving dark half solitons (direction of motion indicated by red arrows), (b) region 3 has vanished after the melting of the surrounding half solitons, (c) region 1 has vanished, resulting in two crossed stationary dark half solitons.

V. SPONTANEOUS FORMATION OF DARK HALF SOLITONS IN THE BISTABLE RANGE

For a scalar self-defocusing Kerr cavity it was previously claimed that pattern formation is frustrated in the bistable pump range, since all patterns are subjected to bistable switching which drives the solution to the stable upper branch of the bistability loop [11].

In the present section, it is shown that the aforementioned bistable switching to the upper part of the bistability loop can be circumvented in the case of vectorial exciton-polaritons according to Eqs. (1). Figure 7 shows the crucial moments of the dynamical evolution near the MI point for $\Delta = -0.7$. After about 900 photon lifetimes the profile shown in Fig. 7(a) consists of three spatially distinct domains designated by 1 to 3. It should be noted that the used split-step Fourier algorithm for numerically solving Eqs. (1) requires periodic boundary conditions. The regions are separated by one-dimensional dark half solitons [39,42]. These half solitons move slowly due to curvature forces [44]. Due to this motion the number of domains will decrease. The domain walls framing the smallest region (in this case region 2) have the largest curvature. This is the reason for the slow movement of these walls in the next step of the dynamical evolution. After about 1500 photon lifetimes they merge eventually [Fig. 7(b)]. The final steady state is reached after about 2300 photon lifetimes with the disappearance of all curved surfaces and of region 1 [Fig. 7(c)].

The formation of these stable patterns depends strongly on external parameters, namely the detunings and the pump power. In order to analyze the stability range of these patterns quantitatively it is useful to have a closer look at the dark half solitons separating the domains in Fig. 7(c). A one-dimensional profile showing both polarizations is depicted in Fig. 8(a). Both polarizations nest on the upper branch of the bistability loop. Whereas $|\Psi^+|$ develops a fully fledged dark soliton, the other polarization $|\Psi^-|$ stays near the HS. This asymmetric configuration is termed half soliton [35,36] or vector soliton [39] and is the only stable soliton for $\alpha < 0$. Dark solitons are usually created by adequately disturbing the upper branch of the bistability loop [39]. The present simulations show that their attraction range in phase space can also be entered from the modulational instability of its lower branch.

In order to form stable dark half solitons in this way, it is therefore necessary to choose a pump power that lies both in the modulationally unstable pump range of the HSs and in the stable pump range of these solitons. The branch of the solitons can be determined by means of the Newton-Raphson iterative method. This method allows for the determination of both stable and unstable solutions depicted in Fig. 8(b) with bold and dashed blue lines, respectively.

The destabilization of a spatially homogeneous flow leading to the formation of spin textured states surrounded by half solitons induced by the instability of a polaritons superfluid has been shown recently in Ref. [21]. The transformation from spin domains to half solitons driven by the transition from linear to nonlinear optical spin Hall effect was shown in Ref. [37]. The formation of a Wigner crystal of half solitons [38] is a further example of self organization of a polarization pattern.

For $\alpha > 0$, the dark soliton solutions to be considered are symmetric [39]. Their stability range is significantly smaller than that of the asymmetric solitons reported for $\alpha < 0$. Particularly, the switching point to the upper branch of the bistability loop lies usually at too high pumps to match this stability range. Therefore, the stabilization mechanism presented in this section was not observed for positive α .

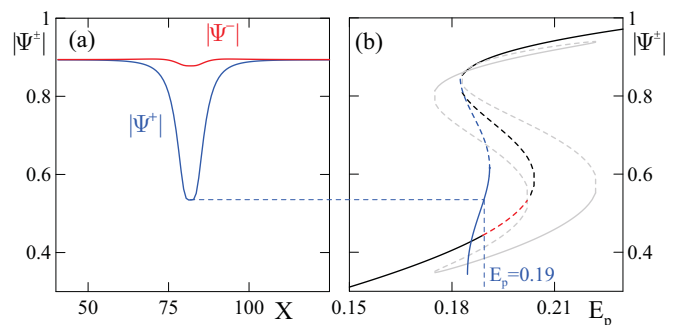


FIG. 8. (Color online) (a) Dark 1D half soliton: slice along dashed line in Fig. 7(c); (b) multistability diagram: symmetric HSs (black), asymmetric HSs (gray), and modulationally unstable HSs (red), stable (unstable) solutions are denoted with bold (dashed) lines, the blue curve denotes the branch $\min|\Psi^-|(E_p)$ of the half soliton in (a). Parameters are $\alpha = -0.1$ and $\Delta = -0.7$.

VI. CONCLUSIONS

In summary, we have studied polariton patterns in a semiconductor microcavity with special emphasis on the spin degree of freedom of these quasiparticles. We found that the sign of the cross-phase modulation parameter α between excitons with different spins is crucial for the topology of the arising patterns. For $\alpha > 0$ all observed patterns are invariant under the permutation of $+$ and $-$. For $\alpha < 0$, however, this spin symmetry is broken spontaneously. This symmetry breaking manifests itself in a spatial shift between the fields with opposite spins. All these simulations were backed by analytical calculations for the corresponding

stationary plane wave solutions, from which the patterns grow spontaneously.

Furthermore we have shown the spontaneous formation of stable domains framed by one-dimensional dark half solitons in the bistable pump range for $\alpha < 0$ and surveyed their properties. This mechanism counteracts the bistable frustration of pattern formation reported for Kerr cavities and spinless polaritons.

ACKNOWLEDGMENT

O.A.E. acknowledges support from the DFG project EG 344/2-1.

-
- [1] C. Weisbuch, M. Nishioka, A. Ishikawa, and Y. Arakawa, *Phys. Rev. Lett.* **69**, 3314 (1992).
- [2] M. S. Skolnick, T. A. Fisher, and D. M. Whittaker, *Semicond. Sci. Technol.* **13**, 645 (1998).
- [3] A. V. Kavokin, J. J. Baumberg, G. Malpuech, and F. P. Laussy, *Microcavities* (Oxford University Press, Oxford, 2007).
- [4] *Exciton Polaritons in Microcavities*, edited by D. Sanvitto and V. Timofeev, Springer Series in Solid-State Sciences Vol. 172 (Springer, Heidelberg, 2012).
- [5] F. Leo, S. Coen, P. Kockaert, S.-P. Gorza, P. Emplit, and M. Haelterman, *Nat. Photonics* **4**, 471 (2010).
- [6] A. Jacobo, D. Gomila, M. A. Matfías, and P. Colet, *New J. Phys.* **14**, 013040 (2012).
- [7] R. Hoyle, *Pattern Formation-An Introduction to Methods* (Cambridge University Press, New York, 2006).
- [8] M. C. Cross and P. C. Hohenberg, *Rev. Mod. Phys.* **65**, 851 (1993).
- [9] L. A. Lugiato and R. Lefever, *Phys. Rev. Lett.* **58**, 2209 (1987).
- [10] J. Y. Courtois and G. Grynberg, *Opt. Commun.* **87**, 186 (1992).
- [11] A. J. Scroggie, W. J. Firth, G. S. McDonald, M. Tlidi, R. Lefever, and L. A. Lugiato, *Chaos, Solitons Fractals* **4**, 1323 (1994).
- [12] J. B. Geddes, J. Lega, J. V. Moloney, R. A. Indik, E. M. Wright, and W. J. Firth, *Chaos, Solitons Fractals* **4**, 1261 (1994).
- [13] J. B. Geddes, J. V. Moloney, E. M. Wright, and W. J. Firth, *Opt. Commun.* **111**, 623 (1994).
- [14] M. Hoyuelos, P. Colet, M. San Miguel, and D. Walgraef, *Phys. Rev. E* **58**, 2992 (1998).
- [15] D. Gomila and P. Colet, *Phys. Rev. E* **76**, 016217 (2007).
- [16] E. Tesio, G. R. M. Robb, T. Ackemann, W. J. Firth, and G.-L. Oppo, *Phys. Rev. A* **86**, 031801(R) (2012).
- [17] H. Saito, T. Aioi, and T. Kadokura, *Phys. Rev. Lett.* **110**, 026401 (2013).
- [18] M. H. Luk, Y. C. Tse, N. H. Kwong, P. T. Leung, P. Lewandowski, R. Binder, and S. Schumacher, *Phys. Rev. B* **87**, 205307 (2013).
- [19] A. Werner, O. A. Egorov, and F. Lederer, *Phys. Rev. B* **89**, 245307 (2014).
- [20] O. A. Egorov, A. Werner, T. C. H. Liew, E. A. Ostrovskaya, and F. Lederer, *Phys. Rev. B* **89**, 235302 (2014).
- [21] H. Terças, H. Flayac, D. D. Solnyshkov, and G. Malpuech, *Phys. Rev. Lett.* **112**, 066402 (2014).
- [22] M. Z. Maialle, E. A. de Andrada e Silva, and L. J. Sham, *Phys. Rev. B* **47**, 15776 (1993).
- [23] K. V. Kavokin, I. A. Shelykh, A. V. Kavokin, G. Malpuech, and P. Bigenwald, *Phys. Rev. Lett.* **92**, 017401 (2004).
- [24] S. Schumacher, N. H. Kwong, and R. Binder, *Phys. Rev. B* **76**, 245324 (2007).
- [25] I. A. Shelykh, A. V. Kavokin, Yuri G. Rubo, T. C. H. Liew, and G. Malpuech, *Semicond. Sci. Technol.* **25**, 013001 (2010).
- [26] I. A. Shelykh, L. Viña, A. V. Kavokin, N. G. Galkin, G. Malpuech, and R. André, *Solid State Commun.* **135**, 1 (2005).
- [27] N. A. Gippius, I. A. Shelykh, D. D. Solnyshkov, S. S. Gavrilov, Yuri G. Rubo, A. V. Kavokin, S. G. Tikhodeev, and G. Malpuech, *Phys. Rev. Lett.* **98**, 236401 (2007).
- [28] S. S. Gavrilov, N. A. Gippius, S. G. Tikhodeev, and V. D. Kulakovskii, *JETP* **110**, 825 (2010) [*Zh. Eksper. Teor. Fiz.* **137**, 943 (2010)].
- [29] T. K. Paraiso, M. Wouters, Y. Léger, F. Morier-Genoud, and B. Deveaud-Plédran, *Nat. Mater.* **9**, 655 (2010).
- [30] I. A. Shelykh, T. C. H. Liew, and A. V. Kavokin, *Phys. Rev. Lett.* **100**, 116401 (2008).
- [31] D. Sarkar, S. S. Gavrilov, M. Sich, J. H. Quilter, R. A. Bradley, N. A. Gippius, K. Guda, V. D. Kulakovskii, M. S. Skolnick, and D. N. Krizhanovskii, *Phys. Rev. Lett.* **105**, 216402 (2010).
- [32] M. Sciamanna and K. Panajotov, *Phys. Rev. A* **73**, 023811 (2006).
- [33] A. Amo, T. C. H. Liew, C. Adrados, R. Houdré, E. Giacobino, A. V. Kavokin, and A. Bramati, *Nat. Photonics* **4**, 361 (2010).
- [34] K. G. Lagoudakis, T. Ostatnický, A. V. Kavokin, Y. G. Rubo, R. André, and B. Deveaud-Plédran, *Science* **326**, 974 (2009).
- [35] H. Flayac, D. D. Solnyshkov, and G. Malpuech, *Phys. Rev. B* **83**, 193305 (2011).
- [36] R. Hivet, H. Flayac, D. D. Solnyshkov, D. Tanese, T. Boulier, D. Andreoli, E. Giacobino, J. Bloch, A. Bramati, G. Malpuech, and A. Amo, *Nat. Phys.* **8**, 724 (2012).
- [37] H. Flayac, D. D. Solnyshkov, I. A. Shelykh, and G. Malpuech, *Phys. Rev. Lett.* **110**, 016404 (2013).
- [38] H. Terças, D. D. Solnyshkov, and G. Malpuech, *Phys. Rev. Lett.* **110**, 035303 (2013).
- [39] A. Werner, O. A. Egorov, and F. Lederer, *Phys. Rev. B* **85**, 115315 (2012).

- [40] P. Renucci, T. Amand, X. Marie, P. Senellart, J. Bloch, B. Sermage, and K. V. Kavokin, *Phys. Rev. B* **72**, 075317 (2005).
- [41] M. Wouters and I. Carusotto, *Phys. Rev. B* **75**, 075332 (2007).
- [42] O. A. Egorov, D. V. Skryabin, and F. Lederer, in *Nonlinear Photonics and Novel Optical Phenomena*, edited by Z. Chen and R. Morandotti, Springer Series in Optical Sciences, Vol. 170 (Springer, Berlin, 2012), p. 171.
- [43] A. M. Turing, *Philos. Trans. R. Soc., B* **237**, 37 (1952).
- [44] D. Gomila, P. Colet, G. L. Oppo, and M. San Miguel, *Phys. Rev. Lett.* **87**, 194101 (2001).